CVD-coated carbon xerogels for negative electrodes of Na-ion batteries

Berke Karaman, Hélène Tonnoir, Da Huo, Bryan Carré, Alexandre Léonard, Jimena Castro Gutiérrez, Marie-Laure Piedboeuf, Alain Celzard, Vanessa Fierro, Carine Davoisne, et al.

▶ **To cite this version:**

Berke Karaman, Hélène Tonnoir, Da Huo, Bryan Carré, Alexandre Léonard, et al.. CVD-coated carbon xerogels for negative electrodes of Na-ion batteries. Carbon, 2024, pp.119077. 10.1016/j.carbon.2024.119077 . hal-04529444

HAL Id: hal-04529444
https://u-picardie.hal.science/hal-04529444

Submitted on 9 Apr 2024

HAL is a multi-disciplinary open access archive for the deposit and dissemination of scientific research documents, whether they are published or not. The documents may come from teaching and research institutions in France or abroad, or from public or private research centers.

L'archive ouverte pluridisciplinaire **HAL**, est destinée au dépôt et à la diffusion de documents scientifiques de niveau recherche, publiés ou non, émanant des établissements d'enseignement et de recherche français ou étrangers, des laboratoires publics ou privés.

CVD-coated carbon xerogels for negative electrodes of Na-ion batteries

Berke Karaman[1], Hélène Tonnoir[2], Da Huo[2], Bryan Carré[1], Alexandre F. Léonard[3], Jimena Castro Gutiérrez[4], Marie-Laure Piedboeuf[1], Alain Celzard[4,5], Vanessa Fierro[4], Carine Davoisne[2], Raphaël Janot[2], Nathalie Job*[1]

[1]*Department of Chemical Engineering - NCE (Nanomaterials, Catalysis, Electrochemistry), University of Liège, 4000 Liège, Belgium*
[2]*Laboratoire de Réactivité et Chimie des Solides - LRCS, UMR7314 CNRS, Université de Picardie Jules Verne, Amiens, France*
[3]*Department of Chemical Engineering - CARPOR, University of Liège, 4000 Liège, Belgium*
[4] *Université de Lorraine, CNRS, Institut Jean Lamour - IJL, 88000 Épinal, France*
[5]*Institut Universitaire de France - IUF, 75231 Paris, France*
*(*corresponding author: Nathalie.Job@uliege.be)*

Keywords: Hard carbon, carbon xerogels, Chemical Vapor Deposition, Na-ion batteries

Abstract

Carbon xerogels (CX) with varying nodule sizes, from 50 nm to 2 µm, are synthesized via polycondensation of resorcinol with formaldehyde in water, followed by pyrolysis at 800 °C to investigate their electrochemical properties as negative electrode material in Na-ion batteries. All samples exhibit high specific surface areas (~600 $m^2\ g^{-1}$ by N_2 physisorption) due to the presence of a large volume of micropores. Chemical Vapor Deposition (CVD) is used to fill or mask the micropores to mitigate the typical detrimental effects of high surface areas on the Initial Coulombic Efficiency (ICE). Larger nodules correlate with increased Na^+ storage capacity and ICE (up to 80 %), independently of the measured specific surface area. Notably, the sample displaying 2 µm nodule size reach a reversible capacity of 248 $mAh\ g^{-1}$ and 80 % ICE at C/20 cycling rate. CVD-deposited carbon layers show a graphitic-like structure and completely block the micropores, reducing the specific surface area and improving both reversible capacity and ICE up to 298 $mAh\ g^{-1}$ and 84 %, respectively. Such materials composed of two different carbons show great promise in the advancement of carbon-based materials for Na-ion batteries.

1. Introduction

The rechargeable battery market is expected to grow dramatically over the next few years, given the demand for electrical energy storage in vehicles, stationary applications and small electronics. [1] This huge deployment, mostly driven by lithium-ion batteries (LIBs), requires the development of new solutions, both in terms of concepts, materials and manufacturing processes, to avoid shortages of key components and ensure that batteries do not become yet another environmental issue. [2][3] In particular, the electrodes must be designed so as to limit the amount of critical materials (i.e., Li, metals such as Cu or Co, and even graphite according to some reports) [4] and non-recyclable compounds such as fluorinated binders (e.g. PolyVinyliDene Fluoride, PVDF) [5]. Finally, the electrode components should ideally be compatible with water-based manufacturing processes, in order to replacing methods using organic solvents (e.g., N-methyl-pyrrolidone, NMP). [5]

Switching from Li-ion batteries (LIBs) to Na-ion batteries (NIBs) would make it possible to get rid not only of Li, which is becoming more and more controversial in terms of availability and extraction impact, but also of Co and Cu and, if properly manufactured, of PVDF and NMP. Indeed, Na is much more abundant in the earth's crust and can be more easily extracted than Li. In addition, since Na does not alloy with Al at low voltage, Cu used for the negative electrodes in LIBs can be replaced by Al and, thus, Al can be used as a current collector for both electrodes. This contributes to a reduction in the price of the final battery. [6] All these reasons make NIBs very good alternative candidates to LIBs from an environmental and cost point of view. However, the energy density of NIBs remains low compared with LIBs (i.e., around 140 Wh kg^{-1} for NIBs against up to 250 Wh kg^{-1} for LIBs) [7]; further research into battery components is thus required to improve energy density.

Carbonaceous materials, mainly graphite, are widely used as negative electrode components in LIBs. However, graphite is unsuitable for NIBs due to poor Na^+ intercalation. Indeed, the electrochemical capacity is limited to ~35 mAh g^{-1}, corresponding to an NaC_{64} stoichiometry, i.e., a stage-8 graphite intercalation compound only. [8][9] For comparison, 370 mAh g^{-1} is reached in the case of Li^+ insertion into graphite (LiC_6). [10] Conversely, non-graphitizable carbons (i.e., hard carbons) are good candidates due to their amorphous structure and large interlayer spacing. Such materials feature randomly oriented turbostratic domains, leading to a large volume of open and closed micropores (i.e., < 2 nm in size) [11][12], suitable for Na storage. Hard carbons can be obtained by pyrolysis of various precursors, mainly oxygen-rich molecules and polymers, which can be bio-based or not. [13]–[15] When used as materials for

NIB negative electrodes, such materials can show reversible capacities of up to 320 mAh g^{-1}. [16] However, their coulombic efficiency at 1st cycle (i.e., the Initial Coulombic Efficiency, ICE) is low due to electrolyte decomposition on their usually highly developed surface area. [17][18] ICE is indeed often directly linked to the carbon specific surface area in the literature: for example, Bommier et al. [19] used hard carbons with total specific surface areas ranging from 25 m^2 g^{-1} to 266 m^2 g^{-1} and observed 80 % and 65 % ICE, respectively. In addition, these materials suffer from poor insertion kinetics: high capacities, up to 300 mAh g^{-1}, have been obtained from pyrolyzed glucose [8][20][21], but only at very low cycling rate (C/80, meaning 80 h to charge or discharge the cell). Finally, their insertion potential is a bit too close to that of Na metal, which might raise safety issues.

Although discussions are still ongoing about Na storage mechanisms in hard carbons, most studies highlight the importance of the pore-filling mechanism by Na^+ ions. In the early 2000s, while studying the galvanostatic profiles of hard carbons (i.e., voltage vs. capacity curves), Stevens and Dahn associated for the first time the low-voltage plateau region (i.e., potential lower than 0.1 V vs. Na^+/Na) with the mechanism of carbon micropore filling by Na^+ ions. [8][20][21] Subsequently, numerous studies have reported similar conclusions that micropore filling is an important storage mechanism in hard carbons. For example, Komaba et al. [22], Stratford et al. [23] or Titirici et al. [24] have all associated the low-voltage plateau with micropore filling. It therefore seems that controlling the microporosity of hard carbons suitable for Na^+ ion storage could be a way of tailoring their electrochemical response. However, it must be noted that increasing capacity and increasing ICE seem to evolve in opposite directions when dealing with microporosity modification. Indeed, as mentioned above, while increasing microporosity can improve capacity, the ICE can in turn drop if the electrolyte can access these micropores. Thus, ideally, and to tackle both issues, the targeted hard carbon should combine (i) a low specific surface area, (ii) a large volume of micropores that the electrolyte itself cannot access, and (iii) a primary particle size compatible with electrode manufacturing and sufficient contact with the electrolyte. In that respect, several methods such as heteroatom doping, surface engineering, pore engineering and so forth have been envisaged in the literature. [25]

For specific surface area and pore engineering, coating techniques have been used to tune the carbon surface properties. For example, Lu et al. [26] coated hard carbons with Al_2O_3 films by atomic layer deposition to develop an artificial SEI layer, leading to both lower BET surface area and pore volume; this strategy improved both the capacity, from 260 mAh g^{-1} to 355

mAh g^{-1}, and the ICE from 67% to 75% (at 20 mA g^{-1}). Additionally, Li et al. [27] used a Chemical Vapor Deposition (CVD) method to modify the surface of sieving carbons; this led to high capacities (up to 390 mAh g^{-1}) with around 80% ICE (at 50 mA g^{-1}); it was claimed that CVD was able to regulate the pore entrance diameter, improving the screening out of solvated sodium ions and enabling the formation of sodium clusters. Therefore, surface and pore engineering of carbons via coatings seems to be an interesting way to improve the capacity and ICE of hard carbons.

Carbon xerogels (CXs) are hard carbons obtained by evaporative drying and pyrolysis of organic gels, e.g., resorcinol-formaldehyde aqueous gels. [28] They are composed of sphere-like microporous nodules, the size of which can be tailored from a few nm to a few µm by modifying the gel composition. [29] Consequently, the meso/macropore texture can also be tailored from a few nm to a few µm. Such carbons have previously been used as negative electrode materials for NIBs [18], but the measured ICE was unsurprisingly low (15 %) given their high specific surface area (~600 m^2 g^{-1}), mainly related to open micropores, while the obtained reversible capacity was reasonably high (~200 mAh g^{-1}). Regarding capacity, it must be noted that the CXs studied so far were mostly made of mesoporous samples, i.e., materials composed of fairly small carbon nodules (~50 nm); to our knowledge, materials made of large carbon nodules (i.e., µm-sized) have not yet been used. It thus seems interesting to investigate the impact of nodule size on electrode performance, especially if large nodules (in the µm range) are used. However, to avoid low ICE, it is also necessary to decrease the surface area accessible to the electrolyte while preserving or even developing closed micropores.

One possible way to reach that goal is to deposit a secondary carbon layer on the surface of CXs nodules by Chemical Vapor Deposition (CVD). In a previous work, Piedboeuf et al. [30] used both physical activation (with CO_2) and CVD (by ethylene cracking) to either increase or decrease the specific surface area of CXs. The initial objective was to analyze the impact of the micropore texture of CXs on their behavior as LIB negative electrode, especially the accessibility of the electrolyte to the carbon surface. Firstly, it was shown that the pore texture of the carbon remained intact in the electrode when using a water-based electrode processing, while the microporosity of the materials was partially blocked when applying a conventional PVDF/NMP processing. As a result, the water-based process developed, using xanthan gum as a binder, is perfectly suitable for studies dealing with the impact of the active material surface area on electrochemical properties. Secondly, it was found that activation indeed increased the accessibility of carbon to the electrolyte, but also that Li^+ ions remained trapped

in the microporosity unless delithiation was performed up to 3 V vs. Li^+/Li, which is totally impractical for real-world applications. Conversely, CVD led to the complete blocking of the micropores, leaving a surface area of about 100 $m^2\ g^{-1}$ corresponding roughly to the external nodule surface. This technique could thus be used to cover the surface of CX nodules in order to decrease the electrolyte/carbon surface contact, and thus increase the ICE for NIBs.

The objectives of this study are therefore (i) to determine the impact of the nodule size of carbon xerogels on their behavior as negative electrodes for NIBs, and (ii) to determine whether the ICE of such materials can be improved by blocking their micropore surface from the electrolyte. To this end, several CXs with various nodule sizes (and thus various meso/macropore textures) were synthesized over a very wide range, especially targeting large nodule sizes (up to a few µm). The same materials were then CVD-coated with carbon to mask the micropores. All the samples were finally processed as electrodes using a water-based technique and xanthan gum as a binder, a method that preserves the pore texture of the powder when processed as an electrode. [31] The obtained electrodes were assembled in half-cell configuration and characterized by electrochemical techniques. The impacts of the nodule size and carbon coating on (i) galvanostatic profile, (ii) ICE, and (iii) rate capability were then determined.

2. Results and discussion

2.1. Physicochemical properties of carbon xerogels

Samples were weighed before and after the CVD procedure to determine the mass increase, which corresponded to 30 %, 19 %, 15 % and 4 % for the samples CX-450, CX-1500, CX-2500 and CX-LPH, respectively. The powders were observed by Scanning Electron Microscopy (SEM) to determine their morphology and nodule size. Figures 1a to 1h show representative SEM images of the four carbon xerogels before and after CVD coating. In all samples, a network of well-connected nodules can be observed, and the size of the nodules, D_n, increases as the *R/C* ratio increases, as expected from data published in the literature. [28] D_n rises from about 50 nm for CX-450 to approximately 1.0 µm, 1.3 µm and 2.0 µm for CX-1500, CX-2500 and CX-LPH, respectively (Table 1). After CVD coating, no significant difference in nodule size is observed. However, some carbon deposits can be seen on samples CX-450-C, CX-1500-C and CX-2500-C (Figure 2a, Figures 1d and 1f), i.e., the three samples

with the highest mass uptake during CVD coating. These deposits seem to consist of small carbon aggregates of various shapes.

Table 1. Pore texture and morphological parameters determined for the four pristine carbon xerogels and their CVD-coated counterparts.

	Morphological parameters				Textural parameters						
					Determined by N_2 adsorption at 77 K			Determined by N_2 and H_2 adsorption at 77 K			
Sample	D_n[a] (μm)	ρ_s[b] (g cm^{-3})	d_p[c] (μm)	$S_{n,ext}$[d] (m² g^{-1})	A_{BET}[e] (m² g^{-1})	S_{ext}[e] (m² g^{-1})	V_μ[e] (cm³ g^{-1})	S_{DFT}[f] (m² g^{-1})	$V_{u\mu,DFT}$[f] (cm³ g^{-1})	$V_{s\mu,DFT}$[f] (cm³ g^{-1})	$V_{T,DFT}$[f] (cm³ g^{-1})
CX-450	0.05	1.93	0.053[f]	91[g]	670	181	0.24	1061	0.16	0.10	0.77
CX-450-C	0.05	1.63			135	118	0.05	145	0.02	0.01	0.44
CX-1500	1.0	1.85	1.4[g]	5[g]	651	-[h]	0.25	1117	0.18	0.10	0.28
CX-1500-C	1.0	1.98			36	-[h]	0.01	191	0.04	0.02	0.09
CX-2500	1.3	1.95	2.6[g]	3[g]	646	-[h]	0.25	1126	0.18	0.11	0.28
CX-2500-C	1.3	2.04			3	-[h]	<0.01	66	0.00	0.02	0.05
CX-LPH	2.0	2.08	3.9[g]	2[g]	643	-[h]	0.25	1113	0.16	0.12	0.28
CX-LPH-C	2.0	1.88			2	-[h]	<0.01	69	0.00	0.02	0.05

[a] D_n: average nodule size calculated from SEM images.

[b] ρ_s: skeletal density measured by He pycnometry.

[c] d_p: pore diameters measured by Hg porosimetry.

[d] $S_{n,ext}$: external surface area calculated from geometric considerations.

[e] A_{BET} and S_{ext}: BET and external surface areas, respectively, and V_μ: micropore volume, calculated from nitrogen adsorption-desorption isotherms at 77 K.

[f] S_{DFT}, $V_{uu,DFT}$, $V_{su,DFT}$, and $V_{T,DFT}$: specific surface area, ultramicropore, supermicropore, and total pore volume calculated from the PSD obtained from nitrogen and hydrogen adsorption isotherms at 77 K.

[g] No significant difference between pristine and CVD-coated materials.

[h] Not measurable.

The XRD patterns of the samples are shown in Figure 3. Note that, given the very small differences observed between CX-450 and CX-LPH or between CX-450-C and CX-LPH-C, the curves obtained with the samples in the middle of the series (CX-1500, CX-2500, CX-1500-C and CX-1500-C), which are quite similar to their pristine or coated counterparts, have been omitted for clarity. Diffractograms of CX-450, CX-450-C, CX-LPH and CX-LPH-C (Figure 3) display a first broad band at around 2θ = 23° (002) and a second broad band around 2θ = 43° (10l), both typical of highly disordered carbon. The (002) band is more intense for CX-450-C and CX-LPH-C than for their uncoated counterparts, which could be due to some coating contribution. The complete structural parameters of coated and uncoated samples are shown in Table 2. Small differences are observed between samples. Indeed, a slightly larger coherence length L_a is observed for CX-LPH-C (3.82 nm vs. 3.38 nm for CX-LPH) and CX-450-C (4.54 nm vs. 3.89 nm for CX-450). One might think that these differences are due to the processing temperature of 900 °C used for the CVD samples. To check this hypothesis, the organic gel prepared at low pH was also pyrolyzed at 900 °C. Figure S.I.1. shows the XRD patterns of CX-LPH pyrolyzed at either 800 °C or 900 °C, as well as that of CX-LPH-C (treated at 900 °C). The patterns of carbon gels pyrolyzed at either 800 °C or 900 °C are very similar. The structural parameters obtained from these three XRD patterns are presented in Table S.I.1. The coherence length L_a obtained for CX-LPH pyrolyzed at 800 °C and 900 °C is very close (3.38 nm and 3.34 nm, respectively), while it is higher for CX-LPH-C (3.82 nm). The increase of L_a value is therefore probably due to pyrolytic carbon deposition. With regard to L_c, the values are very similar for all samples: around 1.0 nm (Tables 2 and S.I.1.). A slight decrease in the graphene interlayer distance, $d_{(002)}$, is observed for CX-LPH-C (0.392 nm vs. 0.405 nm for CX-LPH) and CX-450-C (0.393 nm vs. 0.407 nm for CX-450) (Table 2).

Table 2. Structural parameters of CX-450, CX-450-C, CX-LPH and CX-LPH-C samples.

			CX-450	**CX-450-C**	**CX-LPH**	**CX-LPH-C**
XRD	L_a	(nm)	3.89 ± 0.04	4.54 ± 0.02	3.38 ± 0.01	3.82 ± 0.01
	L_c	(nm)	1.25 ± 0.30	1.12 ± 0.16	1.09 ± 0.19	0.99 ± 0.11
	$d_{(002)}$	(nm)	0.407 ± 0.001	0.393 ± 0.001	0.405 ± 0.001	0.392 ± 0.001
TEM	$d_{(002)}$	(nm)			0.409 ± 0.040	0.392 ± 0.037

To understand better the organization of the carbon layers, CX-LPH and CX-LPH-C were observed by HR-TEM (Figure 4). CX-LPH exhibits a highly disordered structure (Figures 4a and 4b) while its coated counterpart shows a much more ordered and graphitic structure at

some places (Figures 4c and 4d), identified as being close to the nodule surface (Figures 4e and 4f). Numerous alignments of graphene-like sheets a few nm long can be observed after CVD (Figure 4d, orange boxes). The distances between graphene layers determined by TEM are consistent with the results obtained by XRD: the uncoated sample has a higher $d_{(002)}$ value than the coated sample (0.409 nm vs. 0.392 nm, respectively, Table 2). This can be explained by the presence of the carbon layer, which seems to be more ordered according to TEM observations.

As expected, the Hg porosimetry curves performed on the powders show two stages for all samples (Figure S.I.2a): (i) progressive powder compaction at low pressure followed by (ii) a steep intrusion step at higher pressure (marked by arrows in Figure S.I.2a). Pore sizes were calculated from the intrusion step and led to average pore diameters, d_p, of 53 nm, 1400 nm, 2600 nm and 3900 nm for samples CX-450, CX-1500, CX-2500 and CX-LPH respectively (Table 1). No significant modification was observed after CVD treatment (Figure S.I.2b).

N_2 and H_2 adsorption-desorption were used to determine the specific surface area of the samples and gain insight into the micro-mesoporous texture. Results are gathered in Figure 5 and Table 1. Nitrogen adsorption-desorption isotherms are shown in Figure 5a. While the CX-1500, CX-2500 and CX-LPH samples are strictly microporous (type I isotherms), CX-450 also exhibits meso/macroporosity (type I + II isotherm), as suggested by the corresponding SEM micrograph (Figure 1a). The isotherms of the CVD-coated samples show a drastic modification in the low-pressure region corresponding to micropores, in accordance with previous results [30]; this indicates that carbon coating by CVD can be used to block the micropores and reduce the surface area of carbon xerogels, whatever the nodule size. Indeed, A_{BET} calculated from the N_2 adsorption isotherms of the uncoated samples are close (Table 1): 670, 651, 646 and 643 $m^2\ g^{-1}$ for samples CX-450, CX-1500, CX-2500 and CX-LPH, respectively. Calculated values for CVD-coated samples decrease sharply: from 640-650 $m^2\ g^{-1}$ to 36, 3 and 2 $m^2\ g^{-1}$ for samples CX-1500, CX-2500 and CX-LPH, respectively. However, the decrease for the sample CX-450-C is less pronounced (from 670 to 135 $m^2\ g^{-1}$). Accordingly, the micropore volume obtained by the Dubinin-Radushkevich method, V_μ, is almost constant for the pristine carbon xerogels (0.24 – 0.25 $cm^3\ g^{-1}$); it drops to 0.05 $cm^3\ g^{-1}$ for CX-450-C and is below the measurement limit for the other coated samples. Note that V_μ is in fact closely related to A_{BET}: both methods are indeed sensitive to adsorption on the external surface [32] and it is thus normal that they evolve in the same way.

Figure 5b displays the H_2 adsorption-desorption isotherms of the eight samples. The cumulative pore volume as a function of the pore width, *w*, and the derivative pore size distribution (PSD), calculated by combination of N_2 and H_2 adsorption isotherms, are shown in Figures 5c and 5d, respectively. The evolution of the total specific surface area, S_{DFT}, and the pore volume distribution among the mesopores, supermicropores and ultramicropores ($V_{meso,DFT}$, $V_{s\mu,DFT}$ and $V_{u\mu,DFT}$, respectively) upon coating are displayed in Figures 5e and 5f. The H_2 isotherms of the uncoated samples are close again, leading to similar S_{DFT} values: from 1061 to 1126 $m^2\ g^{-1}$ (Table 1). However, the behavior of the coated samples upon H_2 adsorption is quite peculiar. As the nodule size increases, the amount of adsorbed H_2 first increases for samples CX-450-C and CX-1500-C (145 and 191 $m^2\ g^{-1}$, respectively), then drops to 66 and 69 $m^2\ g^{-1}$ in the case of samples CX-2500-C and CX-LPH-C. When detailing the pore volume distribution, one can observe that the CVD coating leads to (i) a loss of 78 – 88 % of $V_{u\mu,DFT}$ for samples CX-450-C and CX-1500-C, (ii) a complete loss of $V_{u\mu}$ for CX-2500-C and CX-LPH-C, and (iii) a decrease between 80 – 90 % of $V_{s\mu,DFT}$ for all samples.

Skeletal density values, ρ_s, measured by He pycnometry, are equal to 1.93, 1.85, 1.95 and 2.08 $g\ cm^{-3}$ for samples CX-450, CX-1500, CX-2500 and CX-LPH, respectively (Table 1). These values are more or less constant and indicate that the structure of the carbon nodules is rather similar, whatever their size. Interestingly, CVD affects the values of ρ_s differently for CX-450 and CX-LPH samples than for CX-1500 and CX-2500 samples. While a decrease in ρ_s is observed after CVD for CX-450 and CX-LPH, a slight increase can be observed for CX-1500 and CX-2500. A possible explanation could be a different pore filling upon CVD for the various materials, depending on both meso/macropore size and nodule size. It is possible that in the case of sample CX-450, which is made of small nodules separated by meso-macropores, some of the spaces between the nodules are blocked by carbon deposits. This would lead to the closure of existing mesopores and a decrease of the skeletal density (Figure 6a). In addition, Figures 2a-b show an irregularly compacted carbon deposit on the surface of the carbon xerogel, with possible gaps beneath the structure. This could also contribute to changes in the material's skeletal density, especially given the high carbon intake upon CVD (30 %). In the case of samples CX-1500 and CX-2500, which have much larger pore sizes and intermediate nodule sizes, carbon deposition by CVD could fill the micropores without clogging the macropores. This filling might not be complete, but given that the carbon deposit is a more ordered structure suggesting a graphitic-like character, and thus denser than the original carbon xerogels, the incomplete filling of the micropores might be compensated,

resulting in an overall increase in skeletal density (Figure 6b). Finally, in the case of the CX-LPH sample, the microporous nodules might be too large to allow the deposition of pyrolytic carbon deep inside the nodules, leading to the formation of closed micropores and a decrease in nodule density (Figure 6c).

All these results show that the CVD coating procedure effectively masks the micropores and certainly fills them, at least in part, with a more ordered carbon, HR-TEM analysis suggesting a graphitic-like character. The latter is further supported by electrochemical measurements, as will be shown in section 2.2.3. Depending on the mass uptake, deposits of irregular shape may also be present, as in sample CX-450-C (Figure 2a). Calculation of remaining surface areas, by distinguishing between the internal and external area of the carbon nodules, might help understanding what surface remains available for the electrolyte in the final electrode. To this end, the external nodule surface area can be determined either by experimental procedures or by geometric calculation. In the case of CX-450 and CX-450-C samples, the external surface area, S_{ext}, was calculated from the N_2 adsorption isotherms using the t-plot method. S_{ext}, which excludes micropores, amounts to 181 $m^2\ g^{-1}$ and 118 $m^2\ g^{-1}$ for CX-450 and CX-450-C, respectively. This seems to show that the CVD coating has little impact on the external surface of the nodules, while all pristine micropores are completely inaccessible. This could correspond to a homogeneous coating of the nodule surface, which is somewhat contradictory to the SEM micrographs where irregular carbon deposits are also seen, and to the hypothesis of mesopore clogging. It is likely that the measured S_{ext} actually corresponds to two contributions: (i) the remaining external nodule surface after clogging and (ii) the additional surface corresponding to irregular carbon deposits (which would compensate for the loss of surface area due to mesopore clogging). In the case of the other samples, the external surface areas of the nodules are too small to be determined accurately by the t-plot method, given the large size of the nodules. However, their values can be estimated by a geometric calculation, considering the micropore volume, V_μ, the nodule size, D_n, and the skeletal density of the carbon material, ρ_s. Indeed, the bulk density of the carbon nodules can be calculated as follows:

$$\rho_{n,bulk} = \frac{1}{V_\mu + \frac{1}{\rho_s}} \quad (1)$$

Then, considering that the nodules are spheres of diameter D_n, the total area corresponding to the outer surface of the nodules can be calculated as follows:

$$S_{n,ext} = n.S_n = nV_n \frac{S_n}{V_n} = \frac{1}{\rho_{n,bulk}} \frac{6}{D_n} \quad (2)$$

where V_n and S_n are the volume and surface area of one nodule, respectively, and n is the number of nodules in 1 g of carbon material. The calculated surface areas (Table 1) are equal to 91, 5, 3 and 2 $m^2 g^{-1}$ for samples CX-450, CX-1500, CX-2500 and CX-LPH, respectively. $S_{n,ext}$ correspond very well to A_{BET} of the CVD-coated samples in the case of CX-2500 and CX-LPH, which indicates that the carbon layer homogeneously covers the surface of the large nodules, as confirmed by the N_2 adsorption data and Figure 2b. $S_{n,ext}$ values are, however, lower than the A_{BET} of CVD-coated samples in the case of CX-1500 and CX-450, which amount to 36 and 135 $m^2 g^{-1}$, respectively. These two samples present the highest mass intake (19 % and 30 %, respectively), which can be explained by the fact that a greater area is available outside the nodules for carbon deposition. This also led to rougher nodule surfaces after CVD treatment, resulting in larger areas measured by N_2 adsorption. The SEM micrographs in Figures 1 and 2 confirm this assumption. It should be kept in mind that the carbon deposition by CVD has not been optimized in terms of mass intake: in the procedure, the deposition time was kept constant. Obtaining a homogeneous coating around the nodules without additional carbon deposits certainly requires precise optimization of the process, which will be the subject of further research.

H_2 adsorption can also help distinguishing between pore filling and pore masking. For CX-450-C and CX-1500-C samples, Figure 5f shows that the CVD treatment leads to the near complete disappearance of the supermicropores, while part of the ultramicroporosity remains present. This corresponds well to a micropore filling mechanism where ethylene fragments cannot access the smallest pores when the nodule size increases, leaving a larger part of the ultramicropores untouched. However, the behavior of samples CX-2500-C and CX-LPH-C remains unexplained. Especially in the case of CX-LPH-C, it seems that coating the nodules with carbon by CVD leaves a significant amount of porosity within the nodules, as deduced from the decrease of the skeletal density (from 2.08 to 1.88 g cm^{-3}, Table 1), but that the carbon layer is not permeable to H_2. In addition, one notes that the mass intake is the lowest of all for that sample (4 %), and that the coating seems very smooth (Figure 2b). This means that the layer deposited is quite thin. Indeed, one can consider that the nodules of sample CX-450 have a bulk density, ρ_{bulk}, of:

$$\rho_{bulk} = \frac{1}{V_{T,DFT} + \frac{1}{\rho_S}} \quad (3)$$

which amounts to 1.3 g cm^{-3} for CX-LPH. If one considers that the nodules are spheres with diameter of 2 µm, and that the mass uptake (4 %) is due to the deposition of a regular carbon layer with a density close to that of graphite (2.2 g cm^{-3}) around the nodule, one can estimate that the maximum layer thickness (i.e., without micropore filling) would be close to 8 nm. Given that the micropores are probably partially filled, the layer is much certainly even thinner, but, to a large extent, impermeable to H_2 and thus without defects or cracks. This astonishing result calls for further investigation to understand properly the exact structure of the CX-LPH composite. Note that in the case of CX-2500-C, the same conclusions may apply; however, the skeletal density increases a little, from 1.95 to 2.04 g cm^{-3}. One must however keep in mind that the mass intake was in that case much higher (15 %), meaning that the micropore masking might be counterbalanced by the addition of carbon with higher skeletal density.

Regarding elemental analysis (Table 3), no significant difference can be observed with the change of nodule size, except in the case of CX-LPH, which has a lower oxygen content: 2.4 wt.% vs. 3.5-3.9 wt.% for the other pristine CXs. For the CVD-coated samples, a clear impact can be observed as all samples display a higher carbon content than their uncoated counterparts (97-98 wt.% vs. 94-96 wt.%); CVD-coated samples contain less oxygen and less hydrogen. Note that Table 3 shows discrepancies between the sum of all element contents and 100 %, typically around 1%. These discrepancies are likely attributable to experimental errors in determining individual element values. Given the sample preparation procedure, the mineral content (unknown) should be extremely low.

Table 3. Elemental analysis of carbon xerogels before and after CVD treatment.

Sample	**N** (wt.%)	**C** (wt.%)	**H** (wt.%)	**S** (wt.%)	**O** (wt.%)
CX-450	0.1	94.1	0.8	0.0	3.5
CX-450-C	0.2	97.3	0.3	0.0	2.2
CX-1500	0.1	94.3	0.7	0.0	3.7
CX-1500-C	0.4	97.5	0.4	0.0	3.3

CX-2500	0.1	94.1	0.8	0.0	3.9
CX-2500-C	0.2	97.5	0.3	0.0	2.1
CX-LPH	0.1	96.2	0.9	0.0	2.4
CX-LPH-C	0.2	98.0	0.3	0.0	2.8

2.2. Electrochemical properties

Following structural and morphological characterization, uncoated and coated samples were electrochemically tested in half-cell configuration to determine their performance as negative electrode materials for Na-ion battery. Figures 7a and 7b show the first galvanostatic charge-discharge curves for pristine and CVD-coated samples, respectively. The same curves comparing directly the same material before and after CVD treatment are displayed in Figures 7c to 7f for better comparison. The corresponding data are summarized in Table S.I.2. The total capacity value at first discharge (e.g., first sodiation) is reported as $C_{tot,disch}$. The reversible capacity (C_{rev}) is the capacity delivered by the first charge (e.g., first desodiation), while the irreversible capacity (C_{irrev}) is the difference between these two values. The ICE was calculated from these values as the ratio between C_{rev} and $C_{tot,disch}$. Finally, the capacities corresponding to the sloping part and to the low-voltage plateau of the first-discharge curve are reported as C_{slope} and $C_{plateau}$, respectively, along with their contribution (in %) to the total first-discharge capacity.

The results of cycling at various C-rates are grouped together in Figure 8, for both uncoated (Figures 8a, c, e and g) and CVD-coated (Figures 8b, d, f, and h) materials. Data are reported in terms of capacities upon sodiation (black) and desodiation (red); the coulombic efficiency at each cycle is also plotted (blue).

2.2.1. Impact of carbon nodule size

The impact of nodule size on the first galvanostatic charge-discharge of uncoated carbon xerogels can be seen in Figure 7a. The first observation concerns the total discharge capacity, which decreases as nodule size increases: from 563 to 312 mAh g^{-1} for samples CX-450 and CX-LPH, respectively. However, the most striking result concerns the ICE (Figure 7a, Table S.I.2). As the nodule size increases, the ICE increases significantly: from 29 to 80 % for samples CX-450 and CX-LPH, respectively. In the literature, the ICE is generally directly

related to the material's specific surface area measured by gas sorption. [33]–[35] However, all the pristine carbon xerogels display similar A_{BET} and S_{DFT} values (Table 1), which precludes any direct impact of total specific surface area on electrolyte decomposition in this case. Nor are the ICE values proportional to the external nodule area; in fact, the ICE seems to correspond to an intermediate area between the external area of the nodule and the total specific surface area determined from gas adsorption. Given that any influence of the binder can be ruled out [31], the only possible explanation is that the electrolyte only partially enters the micropore volume of all materials, and that the volume into which the electrolyte can enter depends on the size of the nodule. For large nodules, the electrolyte would only penetrate the outer fraction of the nodules, while a larger fraction, possibly corresponding to a similar penetration depth, would be accessible in the case of small nodules. Conversely, the entire open micropore volume is accessible to H_2, regardless of nodule size. Therefore, both N_2 and H_2 adsorption fail to predict the solid-electrolyte interphase (SEI) formation area and ICE values, since the calculated surface areas probably do not correspond to the total surface area accessible to the electrolyte. Such a phenomenon was indeed already observed in Li-ion systems, where electrode capacitance was measured using cyclic voltammetry on a symmetric cell made of two identical carbon xerogel-based electrodes [30]: the capacitance was measured proportional to the external surface area of the nodules, and not to the total surface, because the electrolyte could not access the micropores. Determination of the surface area accessible to the electrolyte could be done in the same way in a further study. Another factor that can have an impact on the ICE is the amount of oxygen and heteroatoms in the structure. Indeed, with a higher electronic density, heteroatoms contribute to sodium ad/chemisorption, thus enhancing sodium storage in hard carbons, as described in more detail in the literature, but their amount must be optimized so as not to decrease the ICE too much. [36][37] For the carbon xerogels described in this study, the total amount of heteroatoms, decreases slightly. Especially, the oxygen content drops from 3.5 wt.% for CX-450 to 2.4 wt.% for CX-LPH as the nodule size increases (Table 3). Although the difference is small between the four samples, this may contribute somewhat to the better ICE observed for CX-LPH.

Galvanostatic profiles of uncoated samples display further differences as nodule size increases (Figure 7a). Importantly, CX-450 shows no low-voltage plateau, while the plateau starts to appear in the CX-1500 sample (i.e., 19 mAh g^{-1}, around 6 % of the 1st discharge capacity $C_{tot,disch}$, Table S.I.2.) and continues to increase as nodule size increases, the highest value being obtained for CX-LPH (i.e., 99 mAh g^{-1}, around 32 % of $C_{tot,disch}$). As previously

discussed in the introduction, although the mechanism is the subject of much debate, the low-voltage plateau region is widely attributed to the filling of micropores by Na^+ ions. However, these micropores can only be accessed to by Na^+ ions if the electrolyte does not decompose on their surface, thus filling their volume with SEI. As a result, for carbon xerogels, the appearance and increase of the plateau could correspond to the filling of micropores that remain in the material after their entrance has been filled by SEI, leaving part of the micropore volume untouched. This would explain why no plateau is observed for CX-450, while the plateau lengthens with increasing nodule size. The increase in total reversible capacity can be attributed to the appearance and lengthening of the plateau; indeed, C_{slope} remains similar for all samples while $C_{plateau}$ increases with nodule size.

It must be highlighted that one of the variables that most affects the performance of hard carbons as Na-ion electrode materials is their pyrolysis temperature. [36][38] According to the literature, it may range from 500 °C up to 2500 °C. The performance observed as a function of pyrolysis conditions is difficult to generalize. Tonnoir et al. [10] found that the reversible capacity of non-graphitizing carbons decreases with increasing pyrolysis temperature from 1000 °C up to 2500 °C while Rios et al. [39] suggested that hard carbons produced at low pyrolysis temperatures (below 1000 °C) exhibit both lower reversible capacity (< 200 mAh g^{-1}) and lower ICE (< 50 %). The results seem to be very precursor-dependent, as the final structure of the hard carbons strongly depends on the initial structure of the precursor. [36][38] Here, it is worth mentioning that the pyrolysis temperature was kept low (800 °C), but a reversible capacity as high as 248 mAh g^{-1} with 80 % ICE was obtained. To the best of our knowledge, the values achieved in the present work are the best result ever obtained with such low pyrolysis temperature for hard carbons. It is clear, however, that the key variable for high reversible capacity is nodule size in the case of carbon xerogels. Indeed, for comparison, total capacities of ~400 – 550 mAh g^{-1}, but with only 15 – 30 % ICE, were obtained for carbon xerogels made of nodules around 20-50 nm in size [18]. No plateau was observed in this case, although a higher pyrolysis temperature (1000 °C) was used.

Cycling at different C-rates was performed to understand the relationship between nodule size and rate capability (Figures 8a, c, e and g). First, it must be pointed out that the coulombic efficiency quickly stabilizes at 100 %, except for CX-450 and just after the change in C-rate for the other samples. The capacities reported hereafter are thus considered reversible. When cycling at low C-rates, such as C/20, C/10 and C/5, the capacity trends observed in the first cycle remain the same: the larger the nodule size, the higher the capacity. However, the

situation changes when the C-rate is higher than C/2: the capacity of samples CX-1500, CX-2500 and CX-LPH drops drastically, while that of CX-450 remains fairly stable. CX-450 is the only sample to show a capacity of around 100 mAh g^{-1} at a C-rate of 5C, while the other samples show capacities close to 0 mAh g^{-1}. The reason for this behavior probably lies in the smaller nodule size of CX-450, which provides shorter diffusion paths for Na^+, and is therefore less affected by an increase in C-rate. [40] Additionally, since a larger carbon surface area is accessible to the electrolyte for the CX-450 than for the other samples, electron transfer is facilitated, which limits capacity drops at high C-rate values. After cycling at high C-rates, all samples recover much of their initial capacity: around 83 % for CX-450 after 5 cycles back to C/20, 97 % for CX-1500, 95 % for CX-2500 and 96 % for CX-LPH, showing that the electrode is not degraded at high C-rates. It is also worth mentioning that, for CX-1500, CX-2500 and CX-LPH, the plateau is no longer visible at C-rate values higher than C (Figure S.I.3.a, c, e and g). This is probably due to a difference in kinetics: as the C-rate increases, it becomes more difficult for Na^+ ions to be stored in the inner porosity of the carbon xerogel, far from the nodule surface.

To sum up, both reversible capacity and ICE increase with nodule size, which is most probably related to the fact that the electrolyte does not access the whole volume and surface of the micropores as the nodule size increases. However, smaller carbon nodules perform better at higher C-rates due to shorter pathways and larger exchange areas. Finally, a very high reversible capacity (248 mAh g^{-1}) and a high ICE (80 %) were both achieved in the case of sample CX-LPH, i.e., a carbon material composed exclusively of microporous hard-carbon spheres with a diameter of around 2 µm. To our knowledge, a reversible capacity of 248 mAh g^{-1} and a first-cycle efficiency of 80 % are among the highest values achieved, especially at such a low pyrolysis temperature (800 ºC).

2.2.2. Impact of CVD coating

Figure 7b shows the first galvanostatic charge-discharge curve for all CVD-coated carbon xerogels. This figure, along with the corresponding data reported in Table S.I.2, shows that the total capacity decreases sharply for CX-450-C, does not change much for samples CX-1500-C and CX-2500-C, and increases slightly for CX-LPH-C. The reversible capacity increases after CVD for all samples, except for CX-450 (slight decrease, from 164 to 153 mAh g^{-1}). For CX-1500, CX-2500 and CX-LPH, the increase in reversible capacity is mostly

because the low-voltage plateau lengthens; this could correspond to a significant increase of the volume of closed micropores, inaccessible to the electrolyte but still available for Na^+ storage. For samples CX-450-C, CX-1500-C and CX-2500-C, this goes in line with the evolution of $V_{T,DFT}$ measured by N_2 and H_2 adsorption (Figure 5f, Table 1), which shows that micropores are still present after coating. However, given that the reversible capacity also increases after coating for CX-LPH-C, one can conclude that despite its impermeability to H_2, the coating does not hamper Na^+ insertion. In parallel, all irreversible capacities decrease, and the drop is very pronounced for small nodules (from 398 to 211 mAh g^{-1} for CX-450) while it is quite moderate for large nodules (from 64 to 56 mAh g^{-1} for CX-LPH). This is clearly related to the masking of micropores after CVD, leading to a decrease of both A_{BET} and S_{DFT} (Table 1), and to the fact that the initial micropores are not equally accessible in all uncoated samples. In CX-450, which has small nodules and, presumably, easier access to micropores by the electrolyte, the area on which the SEI may form is greatly decreased after coating. Conversely, in the case of CX-LPH, the micropores are only partially accessible to the electrolyte, and the impact of the carbon coating on the irreversible capacity is lower overall.

In terms of ICE, the increase after coating is especially spectacular for samples CX-1500-C and CX-2500-C, rising from 45 and 63 % to 81 and 79 %, respectively. The ICE of sample CX-450 increases only from 29 to 42 % (with, in reality, a sharp decrease both in total and irreversible discharge capacities). Although the other samples show an increase too, it is not as drastic as for CX-1500 and CX-2500 samples. In the case of CX-LPH, the change is less significant (80 to 84 %) given the already very high ICE for the non-coated material, but most of the increase in total capacity is due to the lengthening of the plateau.

As already pointed out, the carbon coating deposited by CVD has a tremendous impact on the low-voltage plateau region of the galvanostatic profiles for all samples. Indeed, after CVD treatment, the plateau capacity increases from 19 to 88 mAh g^{-1} for CX-1500, from 56 to 75 mAh g^{-1} for CX-2500, and from 99 to 129 mAh g^{-1} for CX-LPH. A short plateau becomes even visible for CX-450. Conversely, the impact observed on the sloping capacity is low for all samples, even though the slope seems more defined for all samples after CVD. It has been reported in the literature that the plateau region capacity seems to correlate with the volume of suitable (micro)pores for sodium storage. [41] Therefore, it can be concluded that CVD leads to the formation of closed pores suitable for Na^+ storage. In the literature, a pore diameter of 1 nm is reported to be the optimum value for promoting the pore-filling mechanism [42].

Cycling at different C-rates was also performed for the CVD-coated samples (Figure 8b, d, f and h). Although the CVD-coated materials display a much higher capacity at slower C-rates (except for CX-450-C), the drop with increasing rate is sometimes more severe compared to non-coated samples. This is the case, for instance, with CX-1500: the coated sample has a higher capacity at C/5 (around 190 mAh g^{-1} for the coated sample vs. around 115 mAh g^{-1} for the uncoated one), but the values almost catch up with those of the uncoated sample at rate C and above. A similar observation can be made for larger nodules. In the case of CX-LPH, the capacity of the coated material may even drop below that of the uncoated one at high C-rate. Moreover, as previously observed for the uncoated sample, the low-voltage plateau disappears for C-rate values above C (Figures S.I.3.b, d, f and h). Capacities are also less stable with the number of cycles (Figures 8b, d, f and h), especially for CX-LPH-C. The reason for this phenomenon has yet to be elucidated, along with the exact nature of the carbon layer given the peculiar H_2 adsorption results obtained for this sample. It most probably depends on the structure of the carbon layer, which in turn needs to be optimized in terms of thickness and structure. Although coated samples seem to be more affected by cycling at high C-rate values than their uncoated counterparts, all samples recover much of their initial capacity after cycling at high C-rate values: around 96 % for CX-450-C after 5 cycles back to C/20, 95 % for CX-1500-C, and 92 % for CX-2500-C. For CX-LPH-C, cycling back to C/20 enables recovery of about 91 % of its initial capacity after 5 cycles, but the capacity drops rapidly to 82 % of its initial value after 60 cycles (i.e., 15 cycles after cycling back to C/20).

2.2.3. Insight into the structure of the carbon layer

Electrochemical characterization in LIB half-cell can also provide some information about the structure of the carbon layer. Indeed, Li^+ ions do insert into graphite below 0.5 V vs. Li^+/Li, while uncoated carbon xerogels show no specific peak, insertion indeed taking place over a very wide voltage range [30]. As mentioned previously, uncoated and CVD-coated CXs have been used in the past as electrode materials for LIBs, in half-cell configuration, in order to understand the role of the micropores on Li^+ storage [31]. On this occasion, cyclic voltammetry was performed but the results on the CVD-coated material were not published at that time. However, these results might prove relevant to the present study.

The samples examined in reference [31], referred to as CX-Ref and CX-CVD for pristine and CVD-coated materials, respectively, are close to CX-450 and CX-450-C (macropore size of

80 nm, CVD treatment of 30 min under the same conditions, leading to a mass increase of 25 %). The electrode preparation was identical to that reported in reference [31] and in the present study. Experimental details are also given in the S.I. Figures S.I.4a and b present the stabilized cyclic voltammetry curves (cycle #10) for the two CX samples, along with the curve shown in reference [31] for graphite. While the uncoated material displays the usual carbon xerogel profile, without clear insertion potential, the coated material exhibits a small peak around 0.25 V vs. Li^+/Li (Figure S.I.4b), exactly where the insertion peak is observed in graphite (Figure S.I.4a). Although this peak is not as sharp as in graphite, its presence in the voltammogram indicates the existence of a graphitic-like structure in the coated CX, which obviously corresponds to the layer deposited by CVD. The layer probably contains many defects, but its position matches that of graphite crystals. Along with the HR-TEM micrographs, this observation suggests that the CVD coating is at least partially graphitized.

3. Conclusions

Carbon xerogels (CXs) with different nodule sizes were synthesized by polycondensation of resorcinol with formaldehyde in water, followed by drying and pyrolysis at 800 °C. The size of the carbon nodules was tailored between 50 nm and 2 µm, while ensuring similar high-specific surface areas, in order to determine its impact on the electrochemical properties of these carbons as Na-ion battery negative electrode materials. The CX nodules were coated with a secondary carbon layer by Chemical Vapor Deposition (CVD) to mask or fill their micropores and improve their Initial Coulombic Efficiency (ICE).

Increasing the nodule size leads to an increase in both total Na^+ insertion capacity and ICE: in particular, ICE values change drastically from 29 % to 80 % as the nodule size increases from 50 nm to 2 µm. In contrast to commonly drawn conclusions in existing literature, ICE appears to be independent of the specific surface area of the sample. This suggests that the surface probed by gas adsorption does not correspond to the surface area accessible to the electrolyte, especially if the nodule size is large. Remarkably, reversible capacity and ICE values of up to 248 mAh g^{-1} and 80 %, respectively, were observed at a cycling rate of C/20 for the sample with the largest nodule size, 2 µm, which is, to the best of our knowledge, unmatched in literature, especially for such a low pyrolysis temperature. Notably, the response of samples at higher C-rates is in the opposite direction, with smaller nodules leading to lower capacity loss, due to the shorter diffusion path length of Na^+ ions inside carbon nodules.

The CVD layer exhibits relatively large graphitic domains on the outer surface of the nodules, and completely masks the microporosity. Indeed, the specific surface area measured by nitrogen adsorption drops from about 600 to 135 m^2 g^{-1} for the sample with 50 nm nodules, and as low as 2 m^2 g^{-1} when the nodule size is 2 µm. ICE increases significantly for all samples, reaching 84 % for the largest nodule size, because the surface area accessible to the electrolyte decreases. The total capacity increases too (up to 298 mAh g^{-1}), and is mainly related to the lengthening of the plateau at low voltage (< 0.1 V vs. Na^+/Na) usually ascribed to the filling of small micropores by Na^+. Thus, the secondary carbon layer deposited by CVD leads to the masking of micropores, consequently expanding the volume of closed micropores suitable for Na^+ storage.

Optimizing CVD coating thickness and carbon xerogel nodule size, while comprehending Na^+ insertion-deinsertion processes through the graphitic-like carbon layer, is expected to pave the way for substantial progress in the engineering of hard carbons for negative electrodes of sodium-ion batteries.

4. Experimental

4.1. Carbon xerogel synthesis

Carbon xerogels (CXs) were prepared following a procedure described in a previous study. [28] First, a 35 wt.% aqueous solution of resorcinol (R) (Merck) was prepared in a sealable glass flask. Then, sodium carbonate (C) (Merck) was added. The *R/C* ratio was used to regulate the nodule size (and thus the meso/macropore size) of the final carbon materials. For this study, four different *R/C* ratios were used: 450 (CX-450), 1500 (CX-1500), 2500 (CX-2500) and infinite (i.e., without sodium carbonate). The latter sample is named low-pH CX (CX-LPH) hereafter. A 37 wt.% solution of formaldehyde was then added to the mixture with a resorcinol/formaldehyde molar ratio of 0.5. The dilution ratio *D*, i.e., the water/reactants molar ratio, was equal to 5.7. The obtained mixture was then magnetically stirred for 1 h. After mixing, the sealed glass flask was put in an oven, at 85 °C and for 72 h, for gelation and aging. Finally, to dry the gel, the container was opened and put in a vacuum oven at 60 ºC. The pressure was progressively decreased down to 12 Pa, and the samples were left to dry overnight.

At the end of drying, organic xerogel monoliths were retrieved. To obtain a narrow final particle size distribution, the materials were ground prior to pyrolysis, following a procedure

from a previous work [31]. After coarse milling by hand in a mortar, the materials were ground to powders using a Fritsch planetary mill (Mono Mill P6). Samples were ground at 400 rpm for 24 cycles of 1 min each, followed by 15 s of rest. Finally, to obtain carbon xerogels, the powders underwent pyrolysis at 800 ºC under N_2 with the following procedure. The temperature was increased to (1) 150 ºC at 1.7 ºC min^{-1} and held for 15 min; (2) from 150 ºC to 400 ºC at 5 ºC min^{-1} and held for 60 min; and (3) from 400 ºC to 800 ºC at 5 ºC min^{-1} and held for 120 min. Finally, the oven was let to cool down to room temperature overnight.

4.2. Carbon coating by CVD

Chemical Vapor Deposition (CVD) was performed in a stainless-steel tubular oven, following the process described in a previous study [30]. First, the temperature of the oven was set at 685 ºC under inert atmosphere (N_2, flow rate: 0.025 mol min^{-1}). Once the oven had reached 685 ºC, the CX powders were introduced into the oven in a quartz boat while using a reverse flow system to maintain the protective inert atmosphere inside the oven. The reactive mixture was then introduced into the system (total flow rate: 0.082 mol min^{-1}), consisting of 80 % ethylene (Air Liquide N25, 0.066 mol min^{-1}) and 20 % nitrogen (Air Liquide Alphagaz 1, 0.016 mol min^{-1}). The CVD treatment time was set at 30 min, and the temperature was maintained at 685 °C. The atmosphere was then changed to 100 % nitrogen (flow rate: 0.025 mol min^{-1}). Finally, after complete purging, the oven temperature was increased to 900 ºC and held for 2 h. Then, the oven was cooled down under nitrogen atmosphere, and the resulting powders were collected. To distinguish uncoated from coated materials, the samples are named as follows: “CX-R/C” for non-coated samples and “CX-R/C-C” for CVD-coated samples.

4.3. Physicochemical characterization of the carbon materials

The pore texture of CX powders was assessed by nitrogen adsorption-desorption measurements. The isotherms were collected at -196 °C using a Micromeritics ASAP 2420 analyzer. Prior to the measurements, the samples were degassed under high vacuum (2×10^{-4} Pa) at room temperature for 5 h and at 270 °C for 2 h. The specific area, A_{BET}, was calculated using the Brunauer-Emmett-Teller (BET) equation, with adsorption data taken over the

relative pressure range of 0.05 to 0.25 for CVD-coated samples and 0.01 to 0.1 for non-coated samples, in order to fulfill the Rouquerol criterion. The micropore volume, V_{μ}, was calculated using the Dubinin-Radushkevich equation. For samples CX-450 and CX-450-C, the external surface area, S_{ext}, corresponding to the nodule surface area (internal micropores excluded), was calculated using the t-plot method. However, this method is unsuitable for the other samples, given their very low nodule external area.

To assess in more detail the microporosity of the materials, hydrogen adsorption-desorption measurements were also carried out. The samples were degassed under high vacuum at 180 °C for 24 h before acquisition of the isotherms at -196 °C using a Micromeritics 3Flex analyzer. The 2D non-local density functional theory for heterogeneous surface (2D-NLDFT-HS) was applied simultaneously to the nitrogen and hydrogen adsorption isotherms using the SAIEUS software from Micromeritics to obtain the pore size distributions (PSDs). Textural properties such as the specific surface area (S_{DFT}), the total pore volume ($V_{T,DFT}$), and the ultramicro-, supermicro- and mesopore volume ($V_{u\mu,DFT}$, $V_{s\mu,DFT}$, and $V_{meso,DFT}$, respectively) were calculated from the obtained PSDs.

Although it provides information about pore texture, the nitrogen adsorption technique is not suitable for its exhaustive determination, since carbon xerogels are simultaneously micro- and meso/macroporous materials. To assess their meso/macropore texture, mercury porosimetry was performed with a Quantachrome Poremaster 60 in a pressure range from 0.01 to 400 MPa. The analysis was carried out for coated and uncoated carbon xerogels in powder form. Analysis of the mercury intrusion data obtained enables pore volume, V_{Hg}, and PSD to be determined for pores with diameters larger than 3.8 nm. The PSD was calculated using the Washburn equation, valid for mercury intrusion without crushing; the values considered for the equation parameters were (i) an average value of liquid/solid contact angle of 140° and (ii) a mercury surface tension of 0.485 N m^{-1}.

The skeletal density of the samples, ρ_s, was measured by He pycnometry using a Quantachrome Ultrapycnometer 1000e, set at a temperature of 20 °C.

SEM was used to observe the carbon morphology and determine the size of the carbon nodules, D_n. Images were obtained using a Tescan CLARA FEG-SEM at 15 kV under high-vacuum conditions. The samples were sputter-coated with gold and mounted with carbon adhesive prior to observation. Average nodule sizes were calculated based on a minimum of 30 measurements per sample. To visualize the microstructure of the CVD-deposited carbon

layer, the CX-LPH and CX-LPH-C samples were observed by transmission electron microscopy (TEM) using a FEI Tecnai F20-S-TWIN microscope and a JEOL JEM-ARM 200F Cold FEG equipped with a spherical aberration probe corrector, both equipment were operated with an acceleration voltage of 200 kV. Samples were prepared by suspending the powder in ethanol. Then, one or two drops of the suspension were deposited on a copper grid with a holey carbon film. High-resolution imaging was performed by controlling the electron dose in order to avoid electron beam-induced artefacts. The d-spacing between graphene layers in the different samples was obtained by Fast Fourier Transform on the HR-TEM images.

X-ray diffraction was used to assess the crystallinity of the materials before and after CVD coating. Measurements were performed in Bragg-Brentano configuration for diffraction angles 2θ between 10° and 80° and a step size of 0.021° with a Bruker AXS D8 Advance diffractometer using a copper X-ray source ($\lambda_{K\alpha}$ = 0.15418 nm). A shallow sample holder with a zero-background single-crystal Si plate was used to minimize sample transparency. The XRD patterns were analyzed using the model developed by Mallet-Ladeira. [43] The average lateral size of the graphene domains (L_a) and the average stacking thickness of the graphene layers (L_c) were determined using Scherrer's equation from reflections (10l) and (002), respectively.

Elemental analysis (EA) was performed in a Vario EL Cube analyzer (Elementar) to measure the bulk C, H, N, S and O contents. Prior to measurements, the samples were dried overnight at 105 °C to remove moisture, and then a small amount of material (~2 mg) was placed in the equipment to be burned in a furnace from which the gas is separated using trapping and chromatographic columns. A thermal conductivity detector quantifies the gases, from which carbon, hydrogen and nitrogen contents can be calculated, with the exception of sulphur being measured with a specific infrared detector. The oxygen content was measured separately in another column using a similar procedure.

4.4. Electrode manufacturing

The electrode manufacturing procedure chosen [30] is known to preserve the pore texture of the carbon material in the electrode configuration, meaning that the carbon specific surface areas measured on both the powder and the final electrode are the same. Additionally, this method avoids the use of toxic solvents and fluorinated polymers as binders. The ink for spray

coating was prepared in MilliQ water with 12 wt.% solids, including carbon xerogels and xanthan gum (Sigma-Aldrich) as a binder, in a weight ratio of 92:8. The mixture was stirred with a magnetic stirrer at room temperature for 3 h. The prepared ink was sprayed onto pre-weighed stainless-steel discs current collectors (Type 304, 15.5 mm, MTI corp.) and dried overnight at 60 °C. The obtained electrodes were then stored in a glove box under Ar. The mass loading of active material ranged from 1.5 mg cm^{-2} to 2 mg cm^{-2} for all samples. It should be noted that the electrodes had to be transferred from one laboratory to another for electrochemical characterization: the electrodes manufactured in the NCE laboratory were thus put back into air, and sent in sealed flasks to the LRCS laboratory. Therefore, before half-cell assembly, and to ensure that all adsorbed water was removed, the electrodes were placed between two glass slides and dried at 110 °C under vacuum in a Büchi glass oven for 12 h.

4.5. Electrochemical characterization

Electrochemical studies were carried out in two-electrode coin-cells (CR2032) using the chosen carbon xerogel as the working electrode, sodium metal (Sigma-Aldrich) as counter and reference electrode, a glass fiber separator (Whatman, 1 mm-thick), and a 1 M solution of sodium hexafluorophosphate ($NaPF_6$, Stella Chemifa) in a mixture of ethylene carbonate and dimethyl carbonate (EC/DMC, Solvionic, 1:1 mass ratio) as the electrolyte (referred to as NP30). The coin cells were assembled in a glovebox under Ar atmosphere (O_2 and H_2O concentration < 1 ppm).

Two series of tests were performed in order to characterize the electrochemical properties of the materials. The first was aimed at evaluating the materials' performance at low C-rates. Therefore, the cells were cycled between 0 V and 2.5 V (vs. Na^+/Na) for 5 cycles at C/20 (which corresponds to 18.6 mA g_{carbon}^{-1}, calculated considering the hypothetical formation of a NaC_6 phase during sodiation with a theoretical specific capacity of 372 mAh g^{-1}), 5 cycles at C/10, 5 cycles at C/5 and then for a further 100 cycles at C/20. A rate of C/n thus corresponds to the insertion of one Na^+ ion for every 6 carbon atoms, in n hours. The second series of tests was designed to evaluate the response of the carbon materials to high C-rates. The first charge/discharge cycles were carried out at a low C-rate (i.e., C/20) to enable the formation of SEI, and then the C-rate was gradually increased to 5C. Thus, the cells were cycled between 0

V and 2.5 V (vs. Na^+/Na) for 5 cycles at C/20, C/10, C/5, C/2, C, 2C and 5C, and then for a further 100 cycles at C/20.

Acknowledgements

N.J. and B.K. would like to thank the F.R.S-FNRS for providing funding as part a PDR project (Convention T.0142.20). R.J., D.H. and H.T. would also like to thank the French Ministry of Higher Education, Research and Innovation (Ministère de l'Enseignement Supérieur, de la Recherche et de l'Innovation, MESRI) for supporting part of this work. IJL team acknowledges the financial support of TALiSMAN and TALiSMAN2 projects funded by ERDF. All the authors thank the platform "Microscopies, Microprobes and Metallography (CC3M)" at the Institut Jean Lamour (Nancy, France) for granting access to TEM facilities.

References

[1] H. Zhang, Y. Huang, H. Ming, G. Cao, W. Zhang, J. Ming, R. Chen, *J Mater Chem A Mater* **2020**, *8*, 1604.

[2] J.F. Peters, M. Baumann, B. Zimmermann, J. Braun, M. Weil, *Renew Sustain Energy Rev* **2017**, *67*, 491.

[3] B.C. Gibb, *Nat Chem* **2021**, *13*, 107.

[4] B.E. Lebrouhi, S. Baghi, B. Lamrani, E. Schall, T. Kousksou, *J Energy Storage* **2022**, *55*, 105471.

[5] D.L. Thompson, J.M. Hartley, S.M. Lambert, M. Shiref, G.D.J. Harper, E. Kendrick, P. Anderson, K.S. Ryder, L. Gaines, A.P. Abbott, *Green Chemistry* **2020**, *22*, 7585.

[6] T. Perveen, M. Siddiq, N. Shahzad, R. Ihsan, A. Ahmad, M.I. Shahzad, *Renew Sustain Energy Rev* **2020**, *119*, 109549.

[7] K. Chayambuka, G. Mulder, D.L. Danilov, P.H.L. Notten, *Adv Energy Mater* **2020**, *10*, 2001310.

[8] D.A. Stevens, J.R. Dahn, *J Electrochem Soc* **2001**, *148*, A803.

[9] P. Ge, M. Fouletier, *Solid State Ion* **1988**, *28–30*, 1172.

[10] H. Tonnoir, D. Huo, C. Davoisne, A. Celzard, V. Fierro, D. Saurel, M. El Marssi, M. Benyoussef, P. Meunier, R. Janot, *Carbon* **2023**, *208*, 216.

[11] C. Bommier, T.W. Surta, M. Dolgos, X. Ji, *Nano Lett* **2015**, *15*, 5888.

[12] D. Saurel, B. Orayech, B. Xiao, D. Carriazo, X. Li, T. Rojo, *Adv Energy Mater* **2018**, *8*, 1703268.

[13] A. Gomez-Martin, J. Martinez-Fernandez, M. Ruttert, M. Winter, T. Placke, J. Ramirez-Rico, *Chem Mater* **2019**, *31*, 7288.

[14] N. Daher, D. Huo, C. Davoisne, P. Meunier, R. Janot, *ACS Appl Energy Mater* **2020**, *3*, 6501.

[15] H. Tonnoir, D. Huo, R.L.S. Canevesi, V. Fierro, A. Celzard, R. Janot, *Mater Today Chem* **2022**, *23*, 100614.

[16] E.M. Lotfabad, J. Ding, K. Cui, A. Kohandehghan, W.P. Kalisvaart, M. Hazelton, D. Mitlin, *ACS Nano* **2014**, *8*, 7115.

[17] L.F. Zhao, Z. Hu, W.H. Lai, Y. Tao, J. Peng, Z.C. Miao, Y.X. Wang, S.L. Chou, H.K. Liu, S.X. Dou, *Adv Energy Mater* **2021**, *11*.

[18] N. Cuesta, I. Cameán, A. Arenillas, A.B. García, *Microporous and Mesoporous Materials* **2020**, *308*.

[19] C. Bommier, W. Luo, W.Y. Gao, A. Greaney, S. Ma, X. Ji, *Carbon N Y* **2014**, *76*, 165.

[20] D.A. Stevens, J.R. Dahn, *J Electrochem Soc* **2000**, *147*, 1271.

[21] D.A. Stevens, J.R. Dahn, *J Electrochem Soc* **2000**, *147*, 4428.

[22] S. Komaba, W. Murata, T. Ishikawa, N. Yabuuchi, T. Ozeki, T. Nakayama, A. Ogata, K. Gotoh, K. Fujiwara, *Adv Funct Mater* **2011**, *21*, 3859.

[23] J.M. Stratford, P.K. Allan, O. Pecher, P.A. Chater, C.P. Grey, *Chemical Communications* **2016**, *52*, 12430.

[24] M.M. Titirici, H. Alptekin, H. Au, A.C.S. Jensen, E. Olsson, M. Goktas, T.F. Headen, P. Adelhelm, Q. Cai, A.J. Drew, *ACS Appl Energy Mater* **2020**, *3*, 9918.

[25] Y. Yang, C. Wu, X.X. He, J. Zhao, Z. Yang, L. Li, X. Wu, L. Li, S.L. Chou, *Adv Funct Mater* **2024**, *34*, 2302277.

[26] H. Lu, X. Chen, Y. Jia, H. Chen, Y. Wang, X. Ai, H. Yang, Y. Cao, *Nano Energy* **2019**, *64*, nwac084.

[27] Q. Li, X. Liu, Y. Tao, J. Huang, J. Zhang, C. Yang, Y. Zhang, S. Zhang, Y. Jia, Q. Lin, Y. Xiang, J. Cheng, W. Lv, F. Kang, Y. Yang, Q.H. Yang, *Natl Sci Rev* **2022**, *9*, 103903.

[28] N. Job, R. Pirard, J. Marien, J.P. Pirard, *Carbon* **2004**, *42*, 619.

[29] A. Arenillas, J. Angel Menéndez, G. Reichenauer, A. Celzard, V. Fierro, F. José, M. Hodar, E. Bailón-Garcia, N. Job, *In:* Organic and Carbon Gels, Advances in Sol-Gel Derived Materials and Technologies Series (Eds: M. A. Aegerter, M. Prassas), Springer, ISBN 978-3-030-13896-7, **2019**.

[30] M.L.C. Piedboeuf, A.F. Léonard, F.L. Deschamps, N. Job, *J Mater Sci* **2016**, *51*, 4358.

[31] M.L.C. Piedboeuf, A.F. Léonard, G. Reichenauer, C. Balzer, N. Job, *Microporous and Mesoporous Materials* **2019**, *275*, 278.

[32] C. Scherdel, G. Reichenauer, M. Wiener, *Microporous and Mesoporous Materials* **2010**, *132*, 572.

[33] R. Alcántara, J.M. Jiménez-Mateos, P. Lavela, J.L. Tirado, *Electrochem Commun* **2001**, *3*, 639.

[34] E.M. Lotfabad, J. Ding, K. Cui, A. Kohandehghan, W.P. Kalisvaart, M. Hazelton, D. Mitlin, *ACS Nano* **2014**, *8*, 7115.

[35] H. Wang, W. Yu, N. Mao, J. Shi, W. Liu, *Microporous and Mesoporous Materials* **2016**, *227*, 1.

[36] X. Dou, I. Hasa, D. Saurel, C. Vaalma, L. Wu, D. Buchholz, D. Bresser, S. Komaba, S. Passerini, *Materials Today* **2019**, *23*, 87.

[37] C. Matei Ghimbeu, J. Górka, V. Simone, L. Simonin, S. Martinet, C. Vix-Guterl, *Nano Energy* **2018**, *44*, 327.

[38] A. Gomez-Martin, J. Martinez-Fernandez, M. Ruttert, M. Winter, T. Placke, J. Ramirez-Rico, *Chemistry of Materials* **2019**, *3*, 7288.

[39] C. del Mar Saavedra Rios, A. Beda, L. Simonin, C.M. Ghimbeu, *In:* Na-Ion Batteries (Eds. L. Monconduit and L. Croguennec), Wiley, **2021**, ISBN 978-1-789-45013-2, Ch. 3, p.101.

[40] H. Hamed, L. Henderick, B.G. Choobar, J. D'Haen, C. Detavernier, A. Hardy, M. Safari, *IScience* **2021**, *24*.

[41] X. Chen, C. Liu, Y. Fang, X. Ai, F. Zhong, H. Yang, Y. Cao, *Carbon Energy* **2022**, *4*, 1133.

[42] X. Dou, I. Hasa, D. Saurel, C. Vaalma, L. Wu, D. Buchholz, D. Bresser, S. Komaba, S. Passerini, *Materials Today* **2019**, *23*, 87.

[43] P. Mallet-Ladeira, PhD thesis, Université Toulouse 3 Paul Sabatier, France, **2014**.

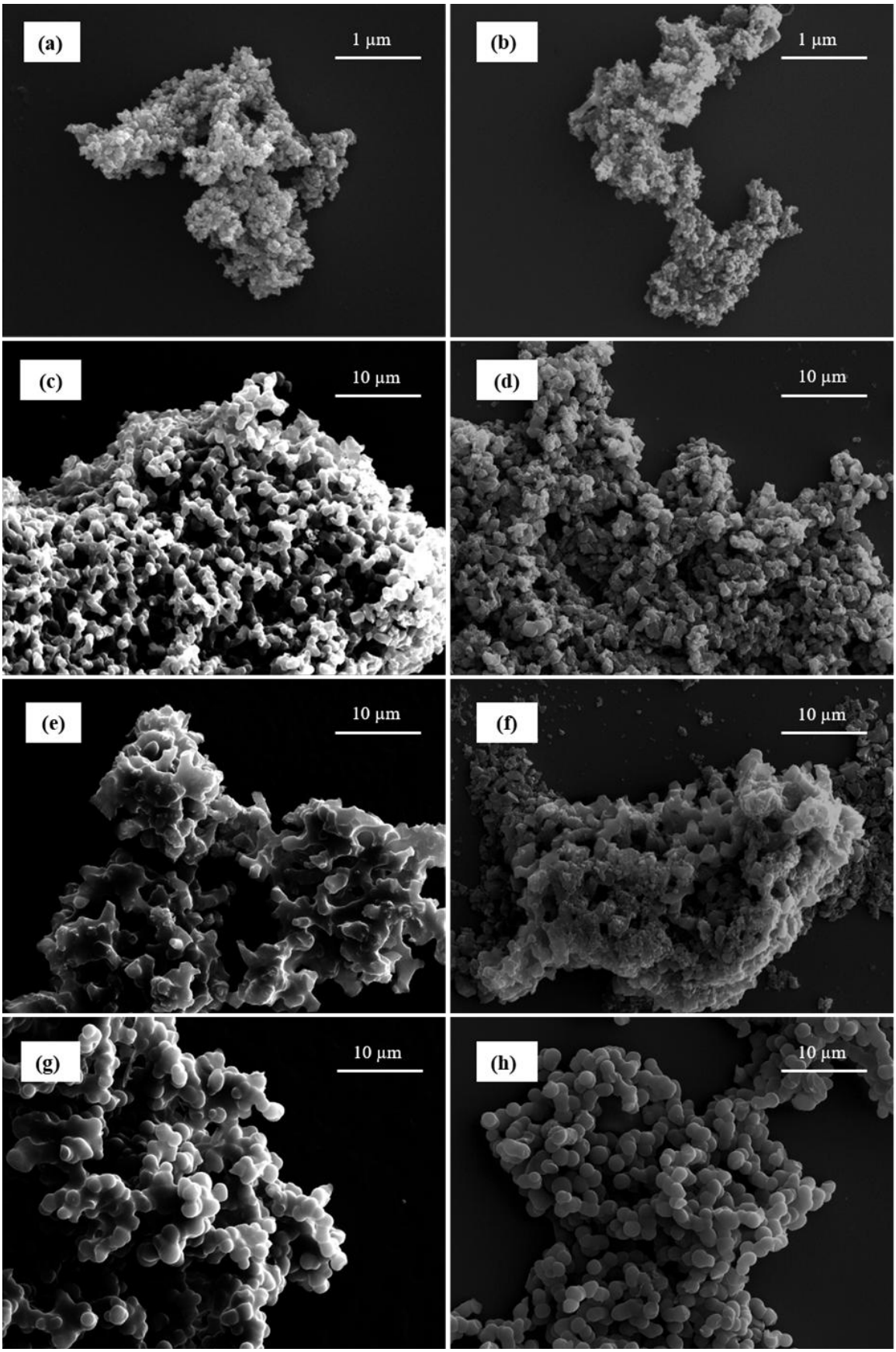

Figure 1. SEM images of (a) CX-450, (b) CX-450-C, (c) CX-1500, (d) CX-1500-C, (e) CX-2500, (f) CX-2500-C (g) CX-LPH, (h) CX-LPH-C.

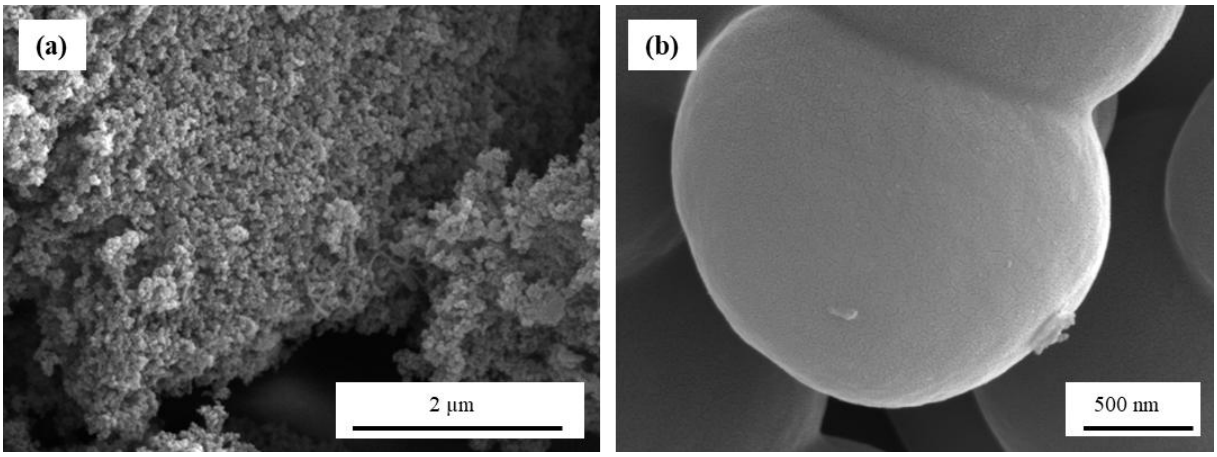

Figure 2. SEM images of (a) CX-450-C and (b) CX-LPH-C at higher magnification.

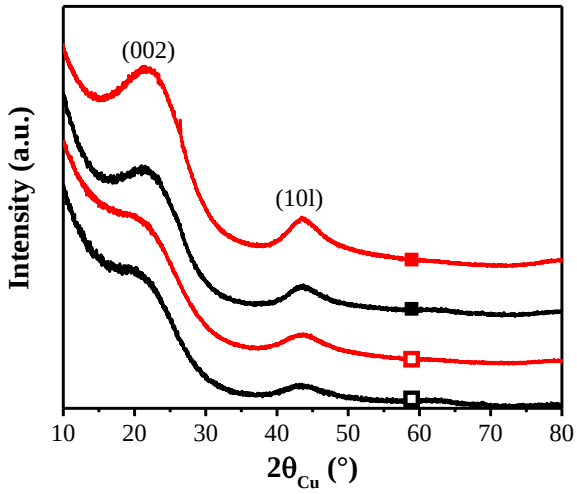

Figure 3. X-ray diffractograms of CX-450 (□), CX-450-C (■) CX-LPH (□) and CX-LPH-C (■).

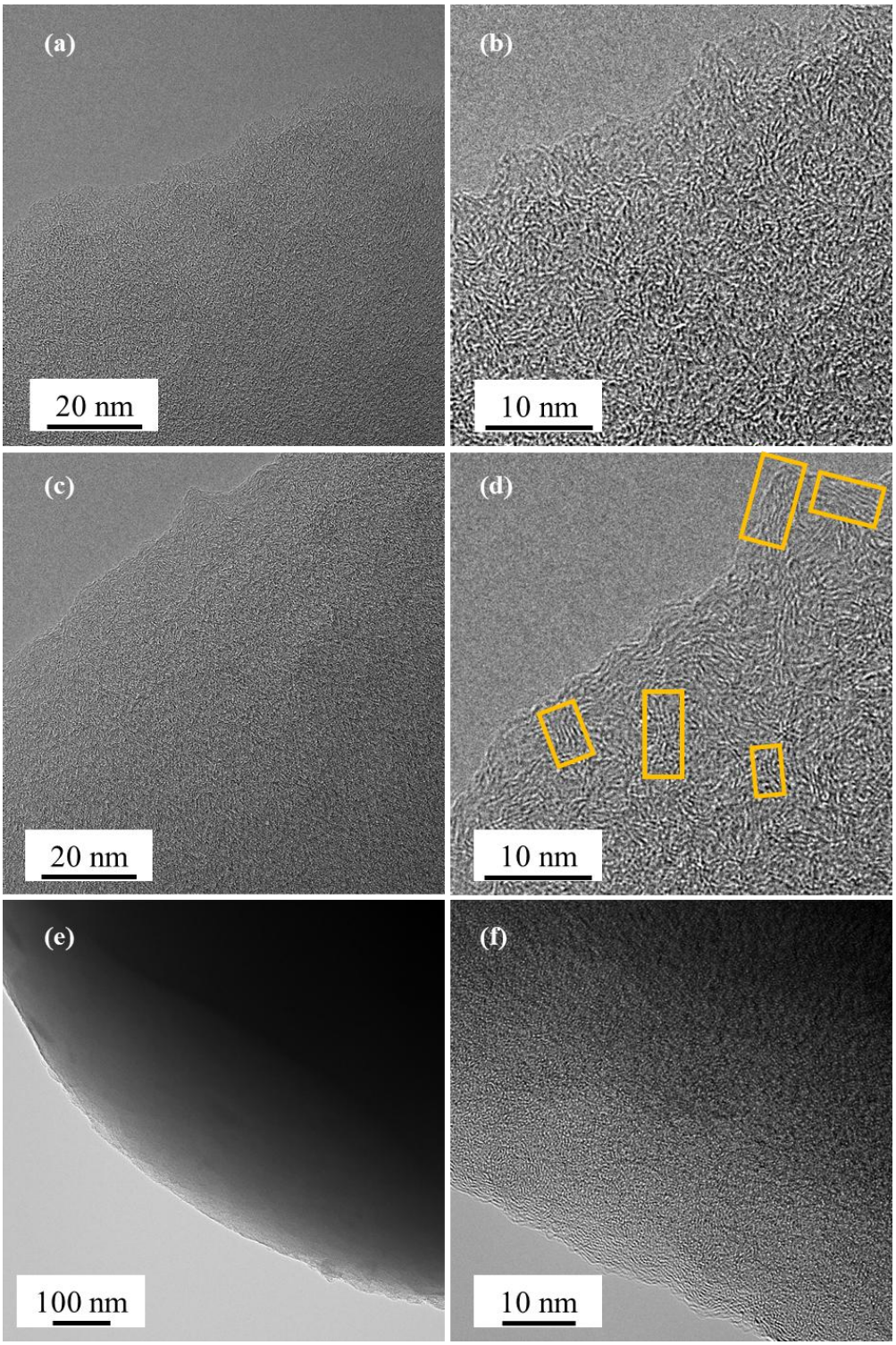

Figure 4. TEM images of (a) and (b) CX-LPH, and (c) and (d) CX-LPH-C. In orange: turbostratic domains. Micrographs (e) and (f) show more precisely the edge of a xerogel particle for sample CX-LPH-C at different magnifications.

Figure 5. Pore texture analysis from gas sorption. (a) N_2 and (b) H_2 adsorption-desorption isotherms of the pristine and coated xerogels. (c) Cumulative and (d) differential pore volume distributions. (e) Total surface calculated by the non-local DFT theory using both N_2 and H_2 adsorption isotherms. (f) Pore volume distribution as a function of their classification. For figures (a), (b) and (c): CX-450 (◇), CX-450-C (◆), CX-1500 (△), CX-1500-C (▲), CX-2500 (□), CX-2500-C (■), CX-LPH (○) and CX-LPH-C (●).

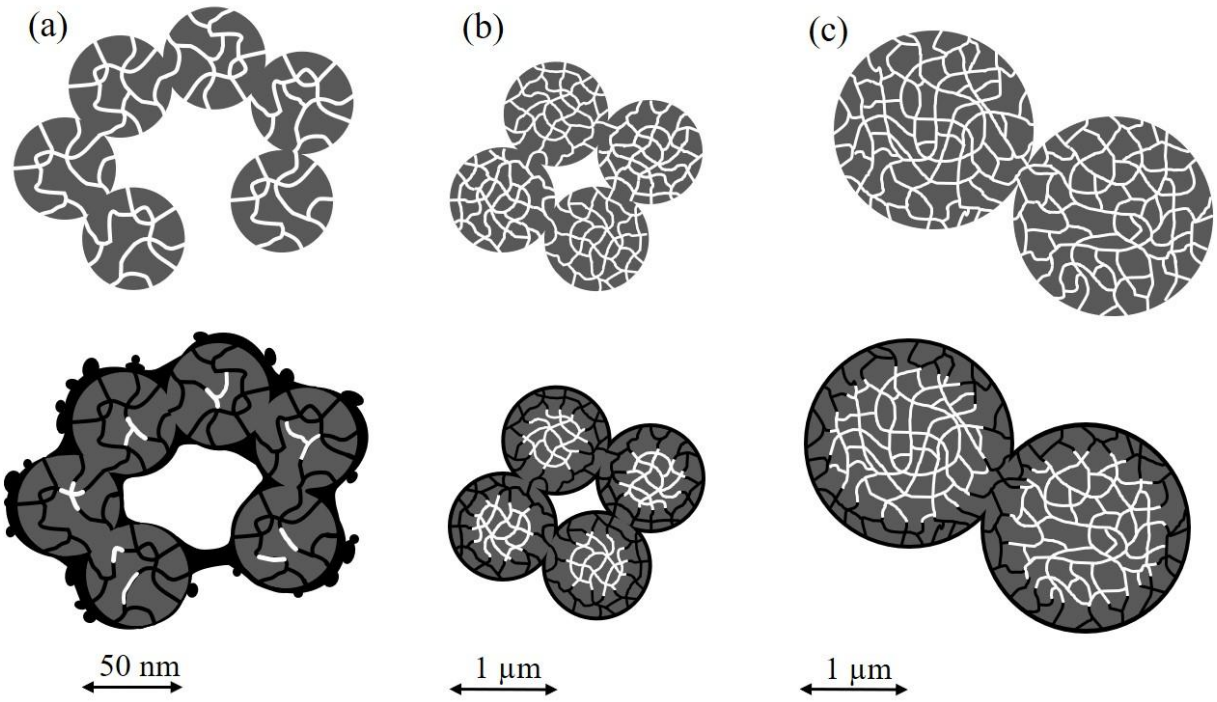

Figure 6. Effect of CVD procedure on the pore texture of carbon xerogels (a) CX-450, (b) CX-1500 and CX-2500 and (c) CX-LPH.

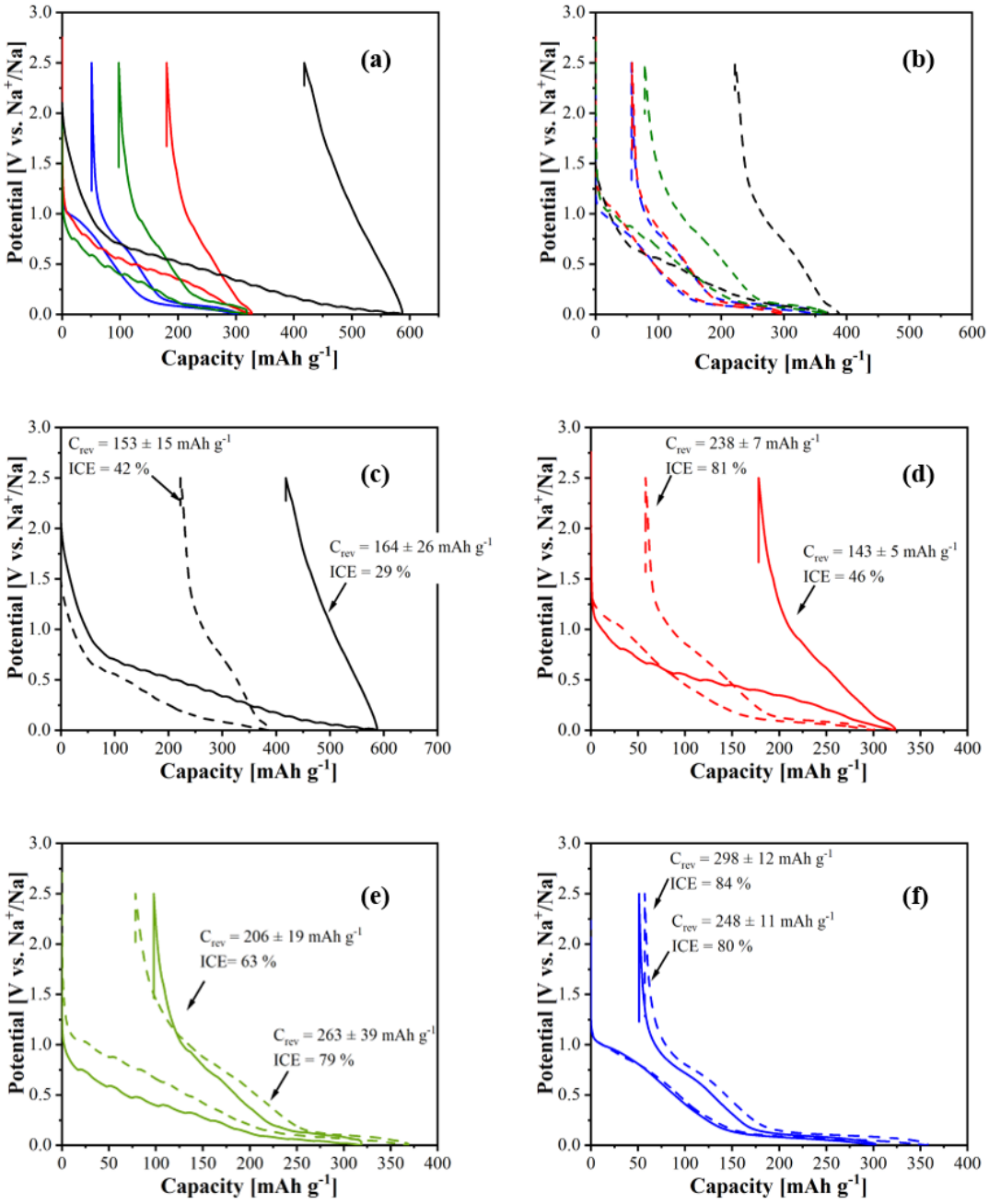

Figure 7. (a) Galvanostatic charge-discharge profiles of the uncoated samples: CX-450 (—), CX-1500 (—), CX-2500 (—), CX-LPH (—). (b) Galvanostatic charge-discharge profiles of the CVD-coated samples: CX-450-CVD (---), CX-1500-CVD (---), CX-2500-CVD (---), CX-LPH-CVD (---). (c-f) First cycle galvanostatic profiles for non-coated (solid) and CVD-coated (dashed) carbon xerogels for the different *R/C* ratio: (c) CX-450, (d) CX-1500, (e) CX-2500 and (f) CX-LPH. Half-cells with NP30 electrolyte, cycling at C/20 (corresponding to 18.6 mA g_{carbon}^{-1}).

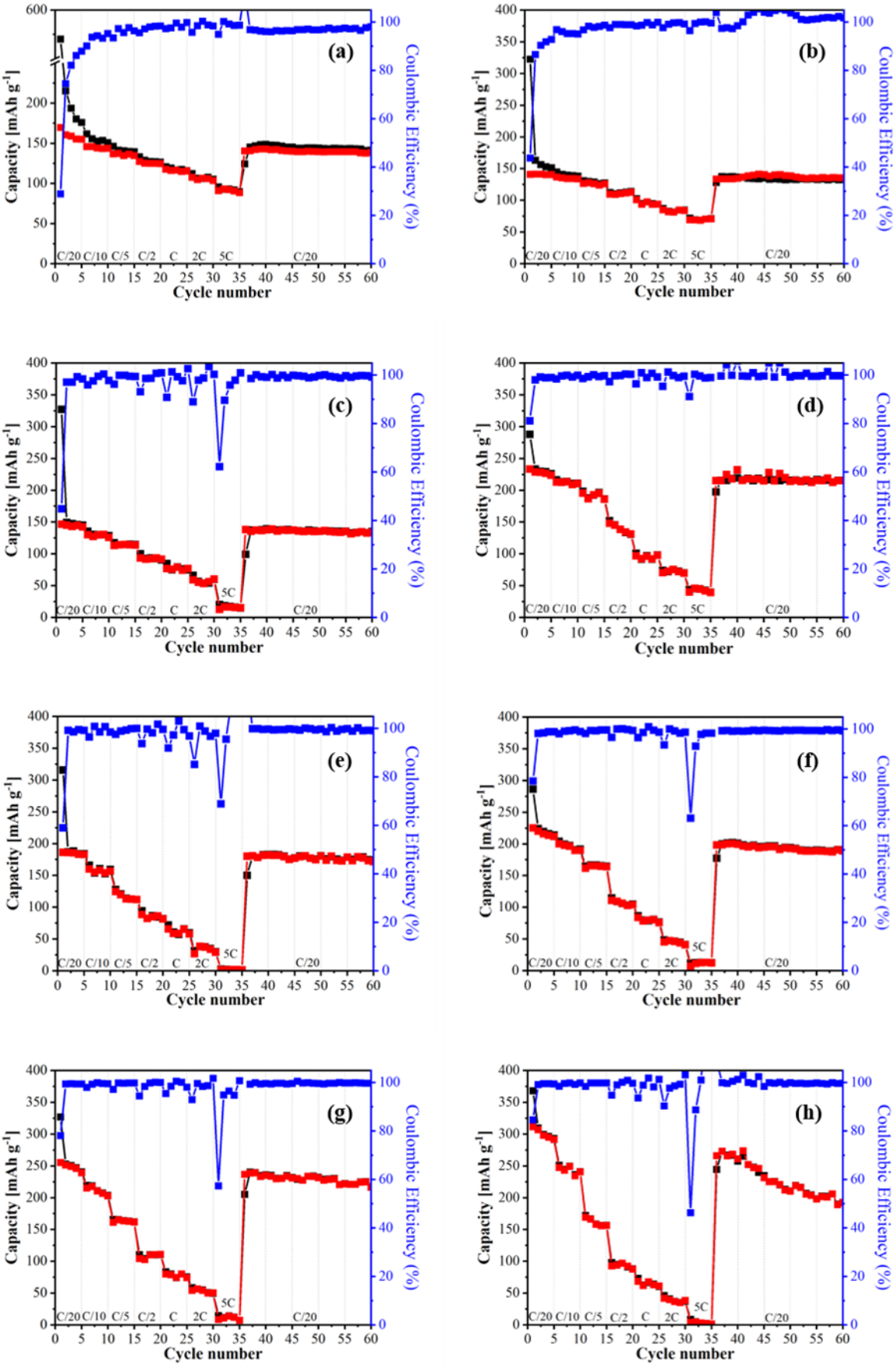
(a)
(b)
(c)
(d)
(e)
(f)
(g)
(h)
Capacity [mAh g-1]
Coulombic Efficiency (%)
Cycle number
C/20 C/10 C/5 C/2 C 2C 5C C/20

Figure 8. Galvanostatic charge-discharge performances according to desodiation capacities (■) sodiation capacity (■) and coulombic efficiency (■). (a) C-450, (b) CX-450-CVD, (c) CX-1500, (d) CX-1500-C, (e) CX-2500, (f) CX-2500-C, (g) CX-LPH, (h) CX-LPH-C at various cycling rates *vs*. coulombic efficiency in each step.